3414 *Chem. Mater.* **2009,** *21,* 3414–3423
DOI:10.1021/cm9011926

CHEMISTRY OF MATERIALS
Article

Preparation of Mesoporous Pt−Ru Alloy Fibers with Tunable Compositions via Evaporation-Mediated Direct Templating (EDIT) Method Utilizing Porous Anodic Alumina Membranes

Azusa Takai,[†] Takahiro Saida,[‡] Wataru Sugimoto,[‡] Liang Wang,[§] Yusuke Yamauchi,*[,†,§,⊥] and Kazuyuki Kuroda*[,†]

[†]*Department of Applied Chemistry and Major in Nanoscience and Nanoengineering, Faculty of Science & Engineering, Waseda University, Ohkubo 3-4-1, Shinjuku, Tokyo 169-8555, Japan,* [‡]*Department of Fine Materials Engineering, Faculty of Textile Science and Technology, Shinshu University, Tokida 3-15-1, Ueda, Nagano 386-8567, Japan,* [§]*World Premier International Research Center for Materials Nanoarchitectonics, National Institute for Materials Science, Namiki 1-1, Tsukuba, Ibaraki 305-0044, Japan, and* [⊥]*Precursory Research for Embryonic Science and Technology, Japan Science and Technology Agency, Kawaguchi, Saitama 332-0012, Japan*

Received April 30, 2009. Revised Manuscript Received June 15, 2009

Synthesis of composition-controlled mesoporous Pt−Ru alloy fibers by a dual-templating method (Yamauchi et al. *J. Am. Chem. Soc.*, **2008**, *130*, 5426−5427) is demonstrated using lyotropic liquid crystals (LLCs) as mesostructural direct templates and porous anodic alumina membranes (PAAMs) as morphological direct templates. The LLCs, including Pt and Ru species, were formed from diluted precursor solutions inside PAAM channels via the evaporation-mediated direct templating (EDIT) method. For all Pt−Ru compositions, the tubular mesophases in the LLCs were stacked like donuts within the PAAM channels because of the confined effect. After metal deposition by the vapor infiltration method of dimethylamineborane (DMAB) and subsequent removal of both surfactants and PAAM, mesoporous Pt−Ru fibers with various compositions were successfully prepared. Both the alloy state and the mesoporous structures were fully characterized by high-resolution scanning electron microscopy (HR-SEM), transmission electron microscopy (TEM), energy-dispersive X-ray spectroscopic (EDS) mapping, X-ray photoelectron spectroscopy (XPS), and electrochemical techniques. The composition ratios of Pt and Ru in the fibers were tuned by controlling those of the used precursor solutions. The mesoporous structures in the fibers reflected the original LLC mesostructures; however, the ordering of the mesoporous structures gradually decreased with the increase in the Ru contents in the precursor solutions.

1. Introduction

Since the discovery of ordered mesoporous silica,[1] many types of mesoporous materials have been synthesized by the supermolecular assembly of surfactants.[2] The framework composition that governs the properties of mesoporous materials has been studied extensively. Mesoporous materials now include a variety of inorganic-based materials, e.g., transition-metal oxides,[3] carbons,[4] inorganic−organic hybrid materials,[5] polymers,[6] and even metals.[7] Because of their metallic frameworks, mesoporous metals with highly

*Corresponding author. E-mail: Yamauchi.Yusuke@nims.go.jp (Y.Y.); kuroda@waseda.jp (K.K.).

(1) Yanagisawa, T.; Shimizu, T.; Kuroda, K.; Kato, C. *Bull. Chem. Soc. Jpn.* **1990**, *63*, 988–992.
(2) (a) Kresge, C. T.; Leonowicz, M. E.; Roth, W. J.; Vartuli, J. C.; Beck, J. S. *Nature* **1992**, *359*, 710–712. (b) Wan, Y.; Zhao, D. Y. *Chem. Rev.* **2007**, *107*, 2821–2860. (c) Inagaki, S.; Guan, S.; Ohsuna, T.; Terasaki, O. *Nature* **2002**, *416*, 304–307. (d) Schüth, F. *Chem. Mater.* **2001**, *13*, 3184–3195. (e) Beck, J. S.; Vartuli, J. C.; Roth, W. J.; Leonowicz, M. E.; Kresge, C. T.; Schmitt, K. D.; Chu, C. T. W.; Olson, D. H.; Sheppard, E. W.; McCullen, S. B.; Higgins, J. B.; Schlenker, J. L. *J. Am. Chem. Soc.* **1992**, *114*, 10834–10843.
(3) (a) Wu, C. W.; Ohsuna, T.; Kuwabara, M.; Kuroda, K. *J. Am. Chem. Soc.* **2006**, *128*, 4544–4545. (b) Fan, J.; Boercher, S. W.; Stucky, G. D. *Chem. Mater.* **2006**, *18*, 6391–6396. (c) Yuan, Q.; Yin, A. X.; Luo, C.; Sun, L. D.; Zhang, Y. W.; Duan, W. T.; Liu, H. C.; Yan, C. H. *J. Am. Chem. Soc.* **2008**, *130*, 3465–3472. (d) Crepaldi, E. L.; Soler-Illia, G. J. A. A.; Grosso, D.; Cagnol, F.; Ribot, F.; Sanchez, C. *J. Am. Chem. Soc.* **2003**, *125*, 9770–9786.
(4) (a) Wan, Y.; Shi, Y.; Zhao, D. Y. *Chem. Mater.* **2008**, *20*, 932–945. (b) Liang, C.; Li, Z.; Dai, S. *Angew. Chem., Int. Ed.* **2008**, *47*, 3696–3717. (c) Wang, X.; Liang, C.; Dai, S. *Langmuir* **2008**, *21*, 11999–12006. (d) Tanaka, S.; Nishiyama, N.; Egashira, Y.; Ueyama, K. *Chem. Commun.* **2005**, 2125–2127.
(5) (a) Inagaki, S.; Guan, S.; Ohsuna, T.; Terasaki, O. *Nature* **2002**, *416*, 304–307. (b) Hoffmann, F.; Cornelius, M.; Morell, J.; Fröba, M. *Angew. Chem., Int. Ed.* **2006**, *45*, 3216–3251. (c) Nicole, L.; Boissière, C.; Grosso, D.; Quach, A.; Sanchez, C. *J. Mater. Chem.* **2005**, *15*, 3598–3627. (d) Shimojima, A.; Kuroda, K. *Chem. Rec.* **2006**, *6*, 53–63.
(6) (a) Meng, Y.; Gu, D.; Zhang, F.; Shi, Y.; Cheng, L.; Feng, D.; Wu, Z.; Chen, Z.; Wan, Y.; Stein, A.; Zhao, D. *Chem. Mater.* **2006**, *18*, 4447–4464. (b) Muylaert, I.; Borgers, M.; Bruneel, E.; Schaubroeck, J.; Verpoort, F.; Van Der Voort, P. *Chem. Commun.* **2008**, 4475–4477. (c) Meng, Y.; Gu, D.; Zhang, F.; Shi, Y.; Yang, H.; Li, Z.; Yu, C.; Tu, B.; Zhao, D. *Angew. Chem., Int. Ed.* **2005**, *44*, 7053–7059.
(7) (a) Attard, G. S.; Bartlett, P. N.; Coleman, N. R. B.; Elliott, J. M.; Owen, J. R.; Wang, J. H. *Science* **1997**, *278*, 838–840. (b) Attard, G. S.; Göltner, C. G.; Corker, J. M.; Henke, S.; Templer, R. H. *Angew. Chem., Int. Ed.* **1997**, *36*, 1315–1317. (c) Warren, S. C.; Messina, L. C.; Slaughter, L. S.; Kamperman, M.; Zhou, Q.; Gruner, S. M.; DiSalvo, F. J.; Wiesner, U. *Science* **2008**, *320*, 1748–1752. (d) Yamauchi, Y.; Yokoshima, T.; Mukaibo, H.; Tezuka, M.; Shigeno, T.; Momma, T.; Osaka, T.; Kuroda, K. *Chem. Lett.* **2004**, *33*, 542–543. (e) Yamauchi, Y.; Kuroda, K. *Chem. Asian J.* **2008**, *3*, 664–676. (f) Yamauchi, Y.; Takai, A.; Komatsu, M.; Sawada, M.; Ohsuna, T.; Kuroda, K. *Chem. Mater.* **2008**, *20*, 1004–1011. (g) Yamauchi, Y.; Takai, A.; Nagaura, T.; Inoue, S.; Kuroda, K. *J. Am. Chem. Soc.* **2008**, *130*, 5426–5427. (h) Yamauchi, Y.; Sugiyama, A.; Morimoto, R.; Takai, A.; Kuroda, K. *Angew. Chem., Int. Ed.* **2008**, *47*, 5371–5373.

Published on Web 07/06/2009

ordered networks and high surface areas hold promise for a wide range of potential applications, such as electronic devices, magnetic recording media, and metal catalysts. An early route to preparing mesoporous metals involves the dealloying of a less noble metal from a bimetallic alloy.[8] This route has been used for the preparation of Raney nickel and other metals.[9] In addition, the electrochemically deposited platinum blacks possess random pores of various sizes and have been used commercially as electrode materials. Compared with the disordered porous metals, ordered mesoporous metals using the supermolecular assembly of surfactants can allow high rates of mass transport and low electrolyte resistance through straight-ordered mesochannels, which are essential for upgrading electrochemical properties.

For a higher specific surface area and higher diffusion efficiency, the morphological controls of ordered mesoporous metals are important. In particular, one-dimensional metals such as fibers and tubes have potential applications for electric wiring and molecular probes because of their high aspect ratios.[10] Recently, we successfully synthesized mesoporous Pt fibers by the dual-templating method utilizing lyotropic liquid crystals (LLCs) as mesostructural direct templates and porous anodic alumina membranes (PAAMs) as morphological direct templates.[7g] The LLC structures inside the PAAM channels showed a physically confined effect leading to the evolution of unique mesostructures such as stacked donut-like tubular mesochannels. This synthetic method should have wide applicability to not only a single system but also alloy systems by the simple addition of several kinds of metal species.[11] The chemical and physical characteristics of the materials are strongly dominated by their metal compositions. Therefore, mesoporous alloy fibers with different metal compositions are vital in order to develop the functionality of nanoscale metals, heighten the specific surface area, and relax the electrolyte diffusion into the mesopores.

In this paper, we demonstrate the preparation of mesoporous Pt−Ru alloy fibers by the reduction of the metal species in the LLCs filled inside the PAAMs. It is well-known that a Pt-based alloy such as Pt−Ru shows higher performance for the electrocatalysis of the oxidation of CO and methanol.[10f,11e,12] Though Pt shows high catalytic activity, the surfaces are strongly poisoned by adsorbed CO molecules. Alloying with Ru increases the CO tolerance because Ru decomposes and releases CO, which is adsorbed on Pt.[10f,11e,12] In this report, we focus on compositional controls in mesoporous Pt−Ru alloy fibers. Tuning of the composition ratios of Pt and Ru on an atomic scale is required for controlled functions.

2. Experimental Procedure

2.1. Materials. Nonionic surfactant ($C_{16}H_{33}(OCH_2CH_2)_8OH$, $C_{16}EO_8$, octaethylene glycol monohexadecyl ether) was purchased from the Fulka Co. Hydrogen hexachloroplatinate(IV) hydrate ($H_2PtCl_6 \cdot 6H_2O$, Kanto Kagaku Co.) and rutheniun-(III) trichloride ($RuCl_3$, Aldrich Co.) were used as Pt and Ru sources, respectively. Ethanol (Junsei Chemical Co.) was used for both the dilution of the precursor solution and the removal of templates. Dimethylamine borane ($(CH_3)_2NH \cdot BH_3$, DMAB) was used as a reducing agent. Porous anodic alumina membranes (PAAMs, Whatman, Anodisc 25, pore diameter ca. 100 nm, thickness 60 μm) were used as hard templates to determine the morphology of the mesoporous fibers. Phosphoric acid (H_3PO_4, Kanto Chemical Co.) was used to dissolve the PAAMs.

2.2. Synthesis of Mesoporous Pt−Ru Alloy Fibers. A diluted precursor solution was prepared by mixing Pt and Ru species for a total amount of 0.28 mmol, including 0.21 g of $C_{16}EO_8$, 0.145 mL of H_2O, and 0.26 mL of ethanol. The solution was dropped on the PAAMs and infiltrated into the PAAM channels. After preferential solvent evaporation, the LLCs on the outer surface of the PAAMs were removed. The PAAMs and 1.0 g of DMAB powder were kept in the same closed vessel (380 mL) at 25 °C for 15 h.[7f,7g] The color of the LLCs in the PAAMs changed from orange to black, indicating Pt and/or Ru deposition in the LLCs. The PAAMs were dissolved by 5 wt % H_3PO_4, and mesoporous fibers of the final products were obtained after washing with water and ethanol.

2.3. Characterizations. The liquid crystalline state of the templating mixtures on a glass slide was confirmed by using an Olympus BX-51 optical microscope under a crossed Nicol field, and the image was recorded on a digital camera. The 2D-XRD patterns were recorded under reflection geometry by a Rint Rapid-S instrument (Rigaku). SEM images were obtained using a Hitachi HR-SEM S-5500 microscope operating at 30 kV. Samples were observed directly without any coatings. TEM images and ED patterns were taken by a JEOL JEM-2010 microscope using an accelerating voltage of 200 kV. Powder samples for the TEM observation were scratched from the substrate and then dispersed in ethanol by ultrasound and mounted on a carbon-coated microgrid (Okenshoji Co.). Energy-dispersive X-ray spectroscopic (EDS) analyses were obtained by a JEOL JSM-6500F scanning electron microscope with an accelerating voltage of 15 kV. XPS analysis was carried out to conclusively investigate the electronic states of the surface

(8) Erlebacher, J.; Aziz, M. J.; Karma, A.; Dimitrov, N.; Sieradzki, K. *Nature* **2001**, *41*, 450–453.
(9) (a) Zhang, X.; Lu, W.; Da, J.; Wang, H.; Zhao, D.; Webley, P. A. *Chem. Commun.* **2009**, 195–197. (b) Snyder, J.; Asanithi, P.; Dalton, A. B.; Erlebacher, J. *Adv. Mater.* **2008**, *20*, 4883–4886. (c) Sun, L.; Chien, C. L.; Searson, P. C. *Chem. Mater.* **2004**, *16*, 3125–3129. (d) Ding, Y.; Kim, Y. J.; Erlebacher, J. *Adv. Mater.* **2004**, *16*, 1897–1900.
(10) (a) Xia, Y.; Yang, P.; Sun, Y.; Wu, Y.; Mayers, B.; Gates, B.; Yin, Y.; Kim, F.; Yan, H. *Adv. Mater.* **2003**, *15*, 353–389. (b) Hurst, S. J.; Payne, E. K.; Qin, L.; Mirkin, C. A. *Angew. Chem., Int. Ed.* **2006**, *45*, 2672–2692. (c) El-Sayed, M. A. *Acc. Chem. Res.* **2001**, *34*, 257–264. (d) Kijima, T.; Yoshimura, T.; Uota, M.; Ikeda, T.; Fujikawa, D.; Mouri, S.; Uoyama, S. *Angew. Chem., Int. Ed.* **2004**, *43*, 228–232. (e) Chan, C. K.; Peng, H.; Liu, G.; McIlwrath, K.; Zhang, X. F.; Huggins, R. A.; Cui, Y. *Nat. Nanotechnol.* **2007**, *3*, 31–35. (f) Liu, F.; Lee, J. Y.; Zhou, W. J. *Small* **2006**, *2*, 121–128.
(11) (a) Yamauchi, Y.; Ohsuna, T.; Kuroda, K. *Chem. Mater.* **2007**, *19*, 1335–1342. (b) Yamauchi, Y.; Sadasivan Nair, S.; Momma, T.; Ohsuna, T.; Osaka, T.; Kuroda, K. *J. Mater. Chem.* **2006**, *16*, 2229–2234. (c) Yamauchi, Y.; Yokoshima, T.; Momma, T.; Osaka, T.; Kuroda, K. *J. Mater. Chem.* **2004**, *14*, 2935–2940. (d) Attard, G. S.; Leclerc, S. A. A.; Maniguet, S.; Russell, A. E.; Nandhakumar, I.; Bartlett, P. N. *Chem. Mater.* **2001**, *13*, 1444–1446. (e) Jiang, J.; Kucernak, A. *Chem. Mater.* **2004**, *16*, 1362–1367.
(12) (a) Marković, N. M.; Gasteiger, H. A.; Ross, P. N., Jr.; Jiang, X.; Villegas, I.; Weaver, M. J. *Electrochim. Acta* **1995**, *40*, 91–98. (b) Gasteiger, H. A.; Marković, N.; Ross, P. N., Jr.; Cairns, E. J. *J. Phys. Chem.* **1993**, *97*, 12020–12029. (c) Lasch, K.; Jörissen, L.; Garche, J. *J. Power Sources* **1999**, *84*, 225–230. (d) Park, K. W.; Choi, J. H.; Kwon, B. K.; Lee, S. A.; Sung, Y. E.; Ha, H. Y.; Hong, S. A.; Kim, H.; Wieckowski, A. *J. Phys. Chem. B* **2002**, *106*, 1869–1877.

of the mesoporous Pt−Ru alloys. XPS spectra were taken at room temperature using a JPS-9010TR (JEOL) instrument with an Mg Kα X-ray source. All binding energies were calibrated by referencing C 1s (285.0 eV).

2.4. Electrochemical Investigations. Cyclic voltammetry was performed by using HZ-3000 and HSV-100 analyzers (Hokuto Denko Corp., Japan). A conventional three-electrode cell, including an Ag/AgCl as the reference electrode and a platinum mesh counter electrode. The mesoporous fibers were dispersed on a glassy carbon electrode which was coated with a solution of 1.0% Nafion and dried at 60 °C for 30 min. The modified glassy carbon electrode was used as the working electrode.

The specific electrochemical surface area was assessed using the CO stripping technique. CO was adsorbed onto the electrode surface by bubbling high-purity CO through the 0.5 M sulfuric acid electrolyte solution for 40 min while holding the potential at 100 mV vs RHE at 25 °C to allow the adsorption of CO to metal surface. After the adsorption process, the dissolved CO was removed from the solution by bubbling high-purity nitrogen for 40 min while holding the potential at 100 mV. The amount of adsorbed CO was evaluated by integration of the CO stripping peak. The resulting current was integrated after correcting for the contribution of the double-layer charging currents. Methanol electro-oxidation measurements were carried out in 0.5 M H_2SO_4 solution containing 1 M methanol by chronoamperometry at 500 mV vs RHE at 60 °C.

3. Results and Discussion

LLCs formed on flat glass substrates before the metal deposition was investigated. The 2D-XRD patterns of the LLCs with various metal compositions are shown in Figure 1. The 2D-XRD patterns for all the LLCs showed four spots assigned to (10), (1−1), (01), and (20) in 2D hexagonal symmetry, with the (10) plane aligned parallel to the substrates.[13] The formation rate of LLCs was investigated by in situ polarized optical microscopic observation (Figure 2). For all samples, no liquid crystallinity was observed at the initial stage. After a few minutes, a typical fan-like texture assignable to a 2D-hexagonal (H_I) mesostructure was observed.[14] However, the formation rates of the LLCs varied depending on the metal compositions of the precursor solutions. The LLC formation rates increased with the Ru contents based on the ligand-exchange reaction rate. LLCs were gradually formed by changing the coordination state of metals during solvent evaporation.[14c] In a previous report by Dag et al., the state of Co species was analyzed during the formation of LLCs starting from $CoCl_2 \cdot 6H_2O$ in a precursor solution.[14c] In their case, the Co species were changed from $[Co(H_2O)_6]^{2+}$ to $[CoCl_4]^{2-}$ and $[Co(H_2O)_4Cl_2]$ by a ligand-exchange reaction. The formation of LLCs was finished when the ligand-exchange reaction between the anion species and coordinating water

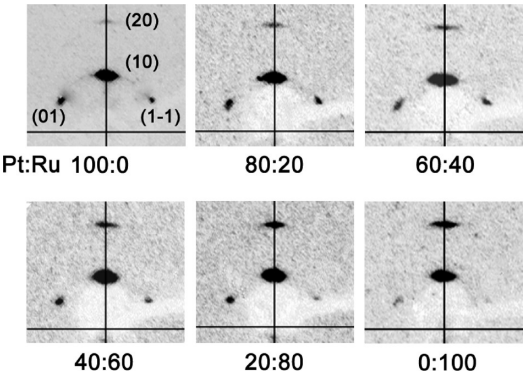

Figure 1. 2D-XRD patterns of LLC mesostructures before metal deposition on glass substrates. The LLC compositions are noted. The lattice planes in 2D hexagonal symmetry were indexed in the pattern of the sample of Pt:Ru = 100:0 as a typical example.

was complete. In the present study, the precursor solutions were composed of water, ethanol as a solvent, and H_2PtCl_6 and $RuCl_3$ as metal species. In general, the ligand-exchange reaction rate of the low-spin d^6 complex is low;[15] that is, the rate of Ru (III) should be faster than that of Pt (IV) because the electron configurations of Ru (III) and Pt (IV) occupy the d^5 and d^6 orbitals of the low-spin complex, respectively. Consequently, the LLC formation rate increases as the Ru ratio increases in precursor solutions.[15] When LLCs formed after the solvent evaporation, the LLC structures were not changed at all. The mesoscopic periodicity of the LLCs was well retained even after 20 h, and no phase separations were observed.

When the LLCs were formed inside the PAAM channels, the 2D-XRD patterns were dramatically changed compared with those of the LLCs on the flat substrates (Figure 3). Two intense spots inclining at ±30° to the out-of-plane direction were clearly observed for all the LLCs inside the PAAM channels. These two spots were assignable to the (10) and (1−1) planes of a 2D-hexagonal mesostructure, indicating that the (10) plane of the hexagonal mesochannels was oriented parallel to the curved PAAM channel surface (i.e., stacked-donut structures).[7g,16] The formation of the unique LLC structures was due to the confined growth effect of the rodlike surfactant assemblies. When the same precursor solution was cast onto the flat substrates, 2D-hexagonal LLC structures with long axes of the rodlike surfactant assemblies were oriented parallel to the substrate surface (Figure 1). Therefore, the confined effect can be considered equivalent to the rolling of a flat substrate surface into a scroll.

In previous reports on the synthesis of MCM-41-type mesoporous silica in PAAM channels, disordered mesostructures were formed in the front surface region of the PAAM channels, though ordered mesostructures were formed in the inner region.[17] In addition, when mesoporous

(13) (a) Miyata, H.; Noma, T.; Watanabe, M.; Kuroda, K. *Chem. Mater*. **2002**, *14*, 766–772. (b) Hillhouse, H. W.; Van Egmond, J. W.; Tsapatsis, M.; Hanson, J. C.; Larese, J. Z. *Microporous Mesoporous Mater*. **2001**, *44*−*45*, 639–643. (c) Yamauchi, Y.; Sawada, M.; Komatsu, M.; Sugiyama, A.; Osaka, T.; Hirota, N.; Sakka, Y.; Kuroda, K. *Chem. Asian J*. **2007**, *2*, 1505–1512.
(14) (a) Dag, Ö.; Alayoğlu, S.; Tura, C.; Çelik, Ö. *Chem. Mater*. **2003**, *15*, 2711–2717. (b) Dag, Ö.; Samarskaya, O.; Tura, C.; Günay, A.; Çelik, Ö. *Langmuir* **2003**, *19*, 3671–3676. (c) Dag, Ö.; Alayolu, S.; Uysal, .I. *J. Phys. Chem. B* **2004**, *108*, 8439–8446.
(15) (a) Yamazaki, K.; Yamadera, H. Muki Kagagaku Bekkan [ge]; Maruzen: Tokyo, 1981. (b) Saito, K. Hatchimentai no Haii Rittai Kagaku; University of Tokyo Press: Tokyo, 1976.
(16) (a) Platschek, B.; Petkov, N.; Bein, T. *Angew. Chem., Int. Ed*. **2006**, *45*, 1134–1138. (b) Platschek, B.; Köhn, R.; Döblinger, M.; Bein, T. *Langmuir* **2008**, *24*, 5018–5023.
(17) Yamaguchi, A.; Uejo, F.; Yoda, T.; Uchida, T.; Tanamura, Y.; Yamashita, T.; Teramae, N. *Nat. Mater*. **2004**, *3*, 337–341.

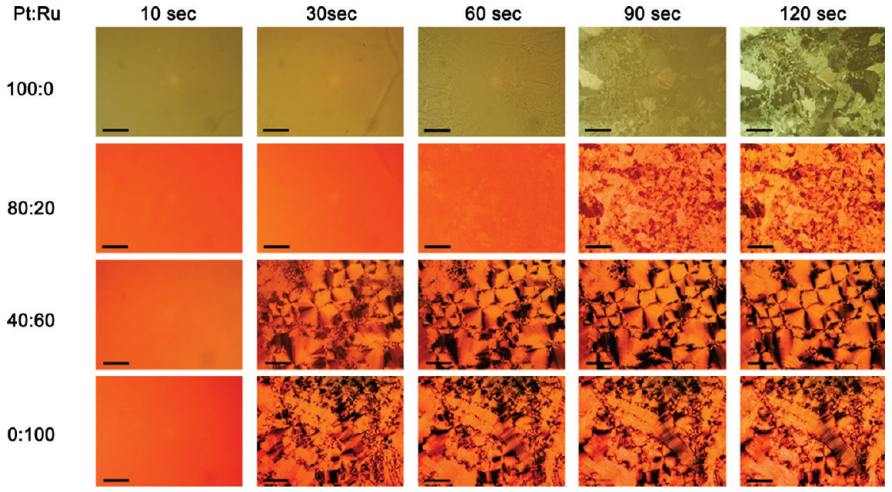

Figure 2. Polarized optical microscopic images of LLC films on glass substrates. The LLC compositions are noted. The scale bar is 200 μm.

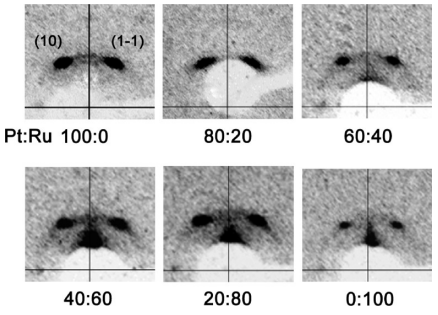

Figure 3. 2D-XRD patterns of LLC mesostructures before metal deposition inside PAAM channels. The LLC compositions are noted. The lattice planes in 2D hexagonal symmetry were indexed in the pattern of the sample of Pt:Ru = 100:0 as a typical example.

titania fibers were prepared inside the PAAM channels, the mesostructural ordering was reduced compared to that of the mesoporous titania films.[18] In these cases, the polymerization of inorganic species (silica and titania) occurs simultaneously with the self-assembly of surfactants by solvent evaporation in which various interactions between the inorganic species and surfactants are inevitable. The obtained mesostructures strongly depend on the sol−gel reaction speeds during the self-assembly of the surfactants. In general, when the sol−gel reactions are terminated before complete evaporation of the solvents, disordered mesostructures are often found.[17,18] Since the evaporation speeds inside confined PAAM channels tend to be slower than those on a flat substrate, the possibility of the formation of disordered mesostructures is higher.

The present EDIT system is different from systems using sol−gel reactions in that the formation speed does not influence the final structure of the LLC mesophase. A homogeneous precursor solution is initially prepared, and then the preferential evaporation of ethanol accelerates to form LLC mesophases (Figure 2). During LLC formation, no chemical reactions among metal species occur. Therefore, the final LLC mesophases after solvent evaporation are predicted by a certain phase diagram of ternary compositions (surfactant + water + metal species).[19] Consequently, highly ordered mesostructures are formed inside the PAAM channels even though the formation rates of the LLCs vary with the Ru contents.

Figure 4 shows SEM images of mesoporous fibers after the removal of surfactants and subsequent dissolution of the PAAM. Regardless of the different alloy compositions, the fiberlike morphology was observed over the entire area. The arrangements of the fibers partially reflected those of the original PAAM channels. EDS mapping images of the mesoporous alloy fibers (prepared from $Pt_{80}Ru_{20}$ precursor solution) are shown in Figure 5. The elemental mappings of both Pt and Ru completely correspond to the dark-field SEM images, proving that the Pt and the Ru atoms were well-dispersed within the fibers without any phase segregation on a nanometer scale.

The XPS spectra of the mesoporous fibers showed two peaks at 71.0 and 74.0 eV, assignable to the Pt $4f_{7/2}$ and Pt $4f_{5/2}$, respectively (Figure 6a). The values of the Pt $4f_{7/2}$ and $4f_{5/2}$ peaks were very close to 70.9 and 74.2 eV for bulk Pt metal,[20] indicating the presence of zerovalent Pt. Regarding the electronic states of Ru, the XPS spectrum was measured in the energy region of 450−490 eV, where Ru 3p peaks were expected to appear because the Ru 3d regions are often obscured by the strong C 1s signal because of surface contamination by carbon. The XPS spectra had two peaks, at 461 and 483 eV, which were assignable to the Ru $3p_{3/2}$ and Ru $3p_{1/2}$, respectively.[20] These spectra indicate that both Pt and Ru exist basically as zerovalents.

The intensities of the Ru 3p peaks increased gradually with an increase of the Ru content in the fibers. The Ru $3p_{3/2}$ signals for the mesoporous $Pt_{62}Ru_{38}$ alloy (prepared from $Pt_{20}Ru_{80}$ precursor solution) and mesoporous Ru fibers were deconvoluted into two peaks with different intensities by using a Gaussian−Lorenz function

(18) Chae, W. S.; Lee, S. W.; Kim, Y. R. *Chem. Mater.* **2005**, *17*, 3072–3074.

(19) Attard, G. S.; Bartlett, P. N.; Coleman, N. R. B.; Elliot, J. M.; Owen, J. R. *Langmuir* **1998**, *14*, 7340–7342.

(20) Wagner, C. D.; Riggs, W. M.; Davis, L. E.; Moulder, J. F. In Handbook of X-ray Photoelectron Spectroscopy; Mullemberg, G. E., Ed.; Perkin-Elmer: Eden Prairie, MN, 1978.

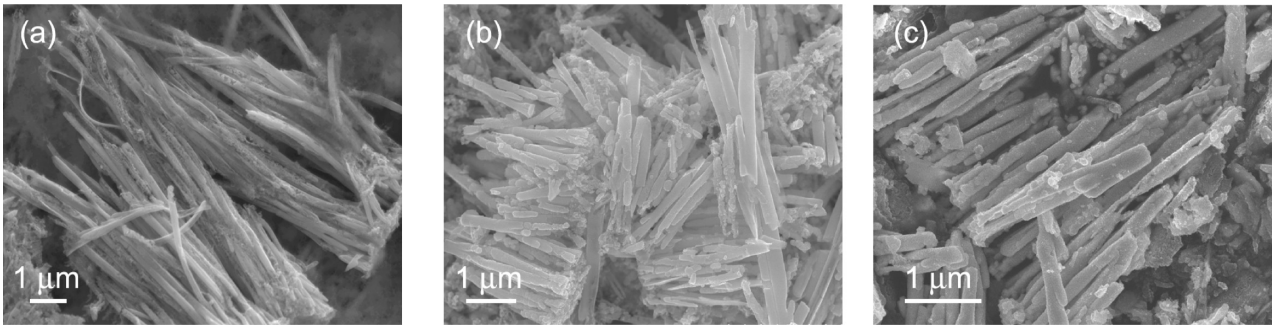

Figure 4. SEM images of mesoporous Pt−Ru alloy fibers synthesized from precursor solutions with metal compositions of (a) Pt_{80}−Ru_{20}, (b) Pt_{40}−Ru_{60}, and (c) Ru_{100}.

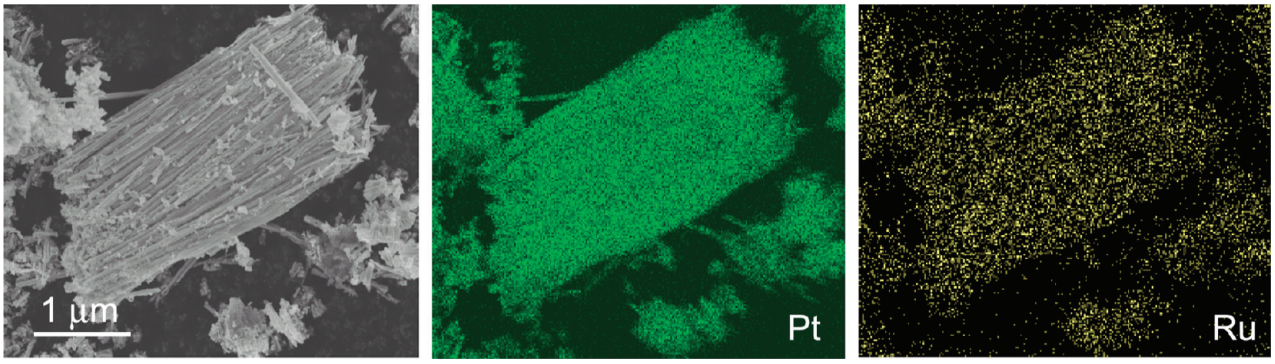

Figure 5. EDS mapping of mesoporous Pt_{86}−Ru_{14} alloy fibers synthesized from Pt_{80}−Ru_{20} precursor solution.

(Figure 6c and 6d). The major peak was located at 462 eV, assigned to Ru^0. The fwhm of the peak was about 5.0 eV, and the value was similar to that of bulk Ru, as reported previously.[21] The other peak, at higher energy (465.2 eV), was attributed to Ru oxide phases such as RuO_2 and RuO_3.[21] On the basis of the integrated peak areas, more than 94 atomic% Ru in the mesoporous $Pt_{62}Ru_{38}$ fiber was present in the zerovalent state (Figure 6c). Though it is well-known that nanosize Ru is easily oxidized in air, the Ru on the surface of mesoporous Pt−Ru alloy was basically zerovalent.

Previously, Jiang and Kucernak reported mesoporous Pt−Ru alloy microspheres from an LLC-templating mixture prepared by heating-aging processes.[11e] It was reported that a high content of O was detected in the resultant mesoporous Pt−Ru alloy by EDX attached to SEM and that the RuO_2 phase was mixed with a Pt−Ru fcc structure in the pore wall. The reported results are quite different from those obtained in the present study, in which most Ru atoms in the mesoporous Pt−Ru alloy fibers were not oxidized. The reason for this difference is not clear at present, but the soft process of solvent evaporation reported here can prevent the formation of Ru oxides. Furthermore, the results of the TEM study (described in detail below) show that the frameworks of the mesoporous fibers were composed of one phase (an fcc structure) as a substitutional solid solution. The complete alloy state can prevent the formation of the Ru oxidized state.

Figure 6e shows the relationship between the precursor compositions and the product compositions estimated by these XPS spectra. No significant increase of the Ru in the products was observed even when the Ru species were highly contained in the precursor solutions. At the 80 at % Ru ratio in the precursor solution, the Ru content in the fibers was dramatically increased to 38 at %. The EDS spectra obtained by using TEM (not shown) were also consistent with the composition ratios estimated from the XPS spectra. The Pt was preferentially deposited because of the difference in the standard electrode potentials of Pt and Ru.[21a] In a previous report on electrodeposited Pt−Ru alloy films under constant potential conditions, the relationship between Ru contents in the deposited alloys and those in the used electrolytes was a third-order polynominal function.[22] The same situation was observed in the present case of the mesoporous Pt−Ru alloy fibers.

The mesostructures inside mesoporous Pt and $Pt_{86}Ru_{14}$ fibers (prepared from $Pt_{80}Ru_{20}$ precursor solution) were investigated using both HR-SEM and TEM (Figures 7, 8, and 9a,b). The mesoporous Pt and $Pt_{86}Ru_{14}$ alloy fibers were composed of the aggregated nanoparticles. The nanoparticles were then joined to make ordered mesostructures, which is typical of metal deposition in LLCs.[7e−7h] The stripes derived from the mesochannels were observed with a repeated distance of about 6 nm. The stripes were oriented perpendicular to the long axis of the PAAM channels. For further investigation of the mesostructures

(21) (a) Milazzo, G., Caroli, S., Eds. Tables of Standard Electrode Potentials; John Wiley & Sons, Ltd.: New York, 1978. (b) Paneva, D.; Tsoncheva, T.; Manova, E.; Mitov, I.; Ruskov, T. *Appl. Catal., A* **2004**, *267*, 67–75. (c) Deshmukh, A. A.; Kinage, A. K.; Kumar, R. *Catal. Lett*. **2008**, *120*, 257–260.

(22) Steen, W. A.; Stork, C. L.; Wall, F. D. *ECS Trans*. **2008**, *6*, 13–27.

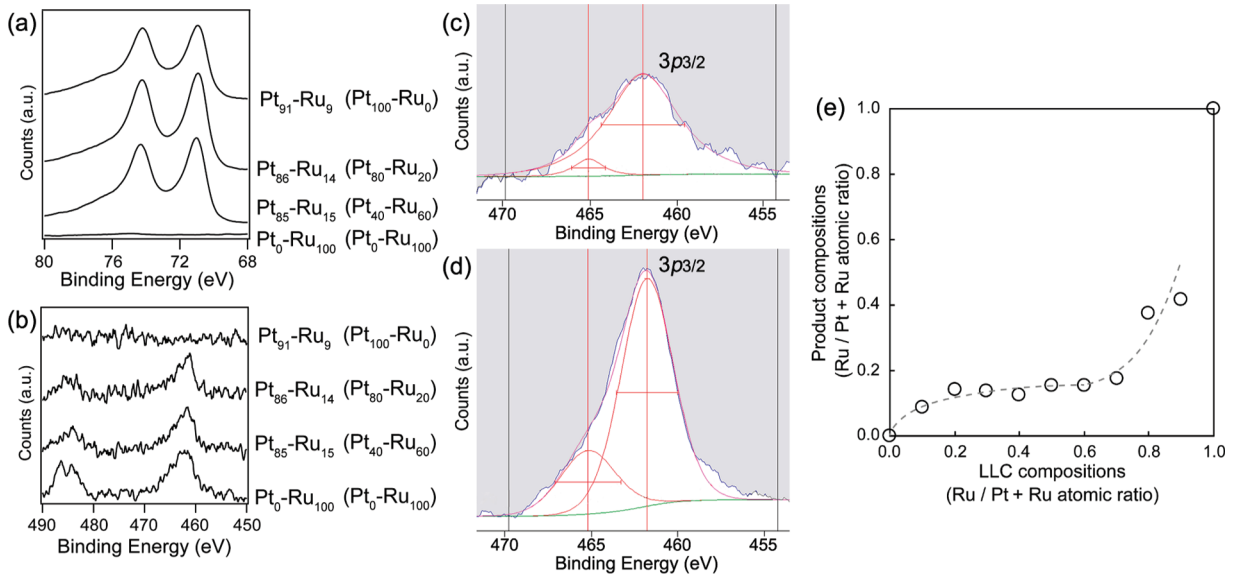

Figure 6. XPS studies of mesoporous Pt, Pt−Ru alloy, and Ru fibers. (a, b) XPS spectra of (a) Pt and (b) Ru for mesoporous Pt, Pt−Ru alloy, and Ru fibers. The product compositions are noted. The compositions shown in parentheses indicate the LLC compositions. (c, d) Deconvoluted XPS spectra of the Ru $3p_{3/2}$ signals by a Gaussian−Lorenz function for mesoporous fibers synthesized from (c) Pt_{20}−Ru_{80} and (d) Ru_{100} precursor solutions, respectively. (e) Relationship of LLC compositions and the product compositions calculated from XPS spectra.

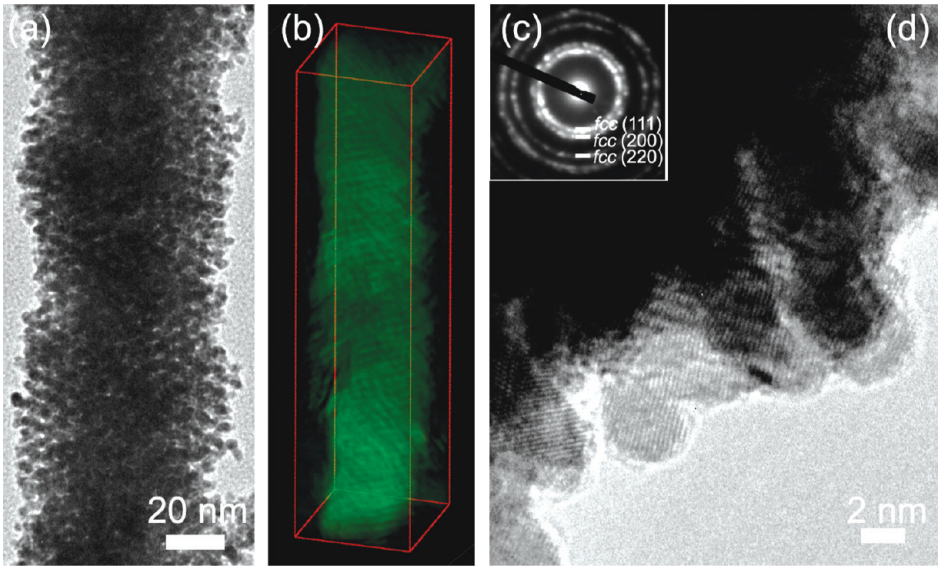

Figure 7. TEM studies of mesoporous Pt fiber. (a) Low-magnified TEM image. (b) Topographical image. (c) Selected-area ED patterns. (d) Highly magnified TEM image.

inside the fiber, three-dimensional (3D) tomography of the Pt fibers was employed by high-angle annular dark-field (HAADF)−scanning transmission electron microscopy (STEM) to obtain valuable spatial information (Figure 7b). The tubular mesochannels were clearly stacked like donuts within the Pt fiber. Therefore, the observed stripes oriented perpendicular to the long axis of the fibers (images a and b in Figure 9) indicated that the tubular mesochannels were circularly formed along the walls of the fibers.[7g] The mesoporous structures in the fibers completely reflected the original LLC mesostructures (Figure 3). However, the 2D-XRD patterns had no obvious spots because X-rays were scattered by heavy metals in lower angle region. Similarly, the $Pt_{86}Ru_{14}$ alloy fibers possessed oriented stripes derived from the stacked donutlike mesochannels. The repeated distance (about 6 nm) was the same as that of the mesoporous Pt fibers. However, as the Ru concentrations were further increased in the precursor solutions, the ordering of the mesostructures inside the fibers decreased. When the Ru contents in the precursor solution were 40 at %, disordered mesostructures consisting of nanoparticles were formed in most parts, though ordered stripe patterns were partially confirmed (images c and d in Figure 9).

The ordering of a mesostructure is strongly related to the metal deposition rate. It was visually confirmed that the metal deposition rate increased with an increase of the Ru concentration in LLCs, which was caused by the

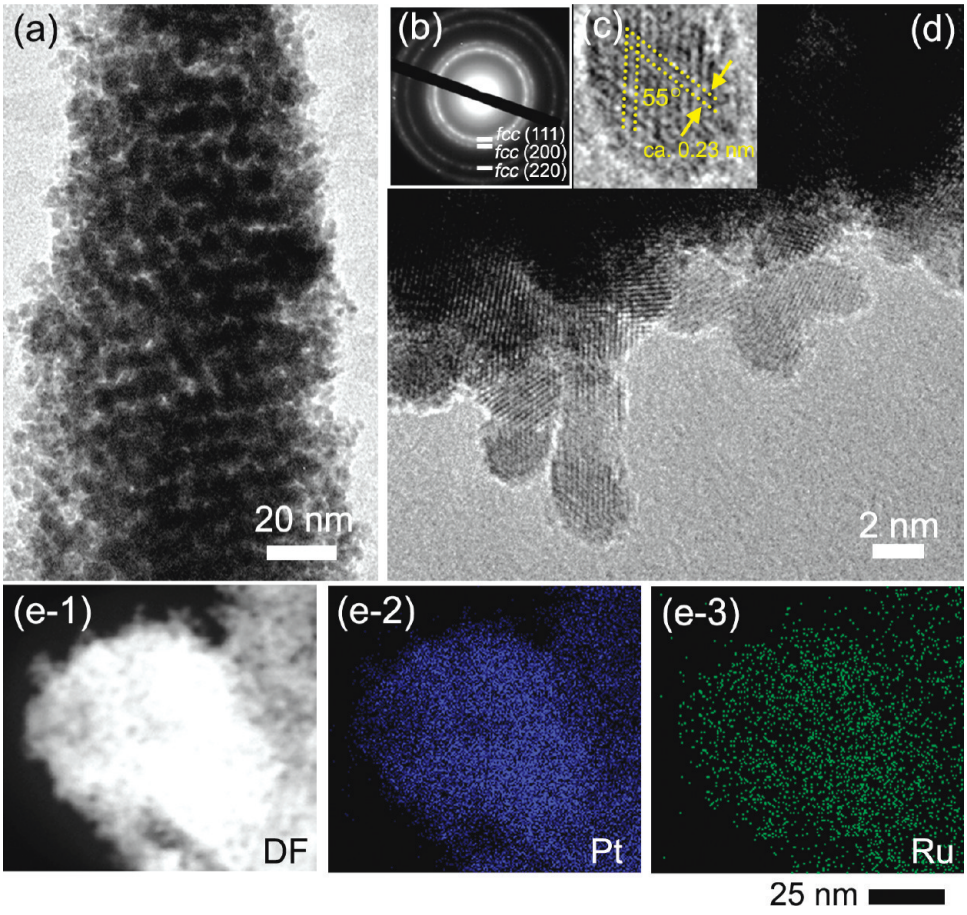

Figure 8. TEM studies of $Pt_{86}Ru_{14}$ alloy fiber synthesized from $Pt_{80}Ru_{20}$ precursor solution. (a) Low-magnified TEM image. (b) Selected-area ED patterns. (c, d) Highly magnified TEM images. (e) EDS mapping. The dark field image (e-1) and the elemental distributions of Pt (e-2) and Ru (e-3).

difference in the catalytic activity of metals for the anodic oxidation of DMAB.[23] The increased rate of metal deposition was insufficient to coat the rodlike self-assemblies in the LLCs. Attard et al. demonstrated the effect of deposition rate on the ordering of a mesoporous structure.[24] In their study, mesoporous Pt films were deposited over a range of potentials (+0.1 V to −0.3 V vs SCE) by the electrodeposition method. When the films were deposited at −0.1 V vs SCE and at potentials more positive (i.e., decreased deposition rates), the XRD patterns exhibited a sharp diffraction peak corresponding to a repeat distance. However, as deposition potentials were decreased (i.e., increased deposition rates), the ordering of the mesoporous structures was gradually reduced.

We further investigated the detailed atomic structure of the framework at a higher magnification. The framework showed a bumpy morphology, proving that the pore wall was composed of connected nanoparticles with an average size of ca. 3 nm (Figures 7d and 8d). The lattice fringes on one nanoparticle corresponded to the {111} planes because both *d*-spacings were 0.23 nm and the dihedral angle was ca. 55°, indicating that each nanoparticle had single crystallinity with an fcc structure (Figure 8c). The selected-area ED pattern from a 100 nm region showed the ring patterns, each of which was assignable to the (111), (200), or (220) lattice plane of the fcc structure (Figures 7c and 8b). The presence of other phases (e.g., $PtRu_3$ and PtRu (ordered structures) and Ru oxides) was not confirmed (Figure 8b). The lattice fringes were randomly oriented across the connected nanoparticles. The observed ED pattern had diffused rings and intense points located on the rings. The sizes of the domains with single atomic crystallinity varied from 3 to 10 nm or more, equal to 1−3 nanoparticles or more. The recording of the intense diffraction points was attributed to the coexistence of such large crystals. With the increase of the Ru content in the fibers, the intense spots disappeared and the brightness of the ED patterns weakened, indicating that the single domain size was gradually reduced. The codeposition of two metal species with different standard electrode potentials (E_0) (Pt, 1.19 V; Ru, 0.46 V[21a]) may have affected the reduction of the domain size of the single atomic crystallinity. It has been reported that electrodeposited Pt-group alloy nanoparticles (e.g., Pt−Ru, Pt−Ru−Ni) prepared in the absence of surfactants possess a smaller atomic crystalline size compared to Pt alone.[25] The same

(23) Ohno, I.; Wakabayashi, O.; Haruyama, S. *J. Electrochem. Soc.* **1985**, *132*, 2323.
(24) Elliott, J. M.; Attard, G. S.; Bartlett, P. N.; Coleman, N. R. B.; Merckel, D. A. S.; Owen, J. R. *Chem. Mater.* **1999**, *11*, 3602–3609.
(25) (a) Park, K. W.; Choi, J. H.; Kwon, B. K.; Lee, S. A.; Sung, Y. E.; Ha, H. Y.; Hong, S. A.; Kim, H.; Wieckowski, A. *J. Phys. Chem. B* **2002**, *106*, 1869–1877. (b) Liu, Z. L.; Ling, X. Y.; Su, X. D.; Lee, J. Y.; Gan, L. M. *J. Power Sources* **2005**, *149*, 1–7. (c) Huang, J. C.; Liu, Z. L.; He, C. B.; Gan, L. M. *J. Phys. Chem. B* **2005**, *109*, 16644–16649.

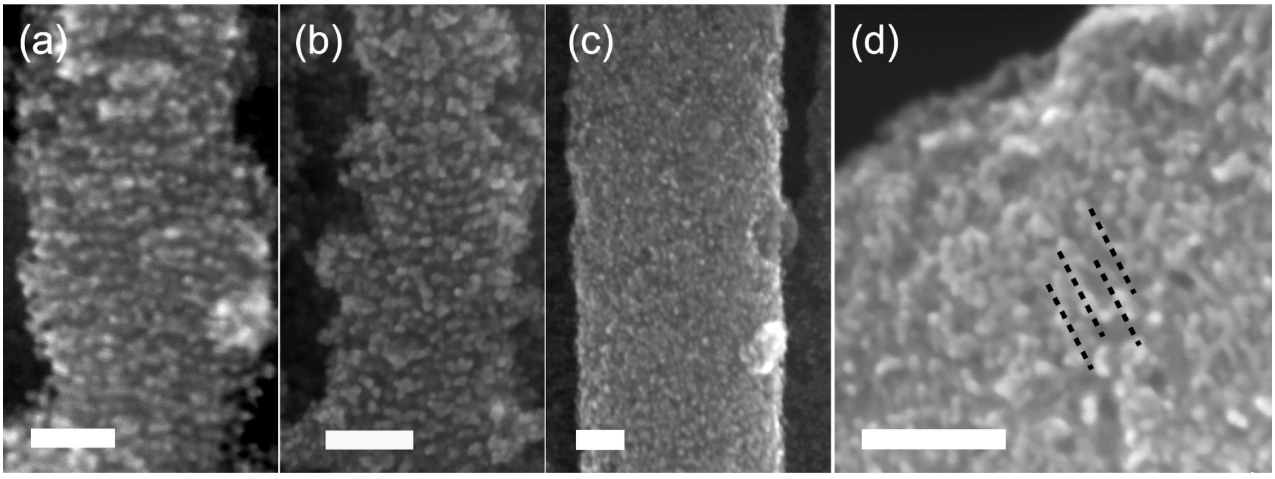

Figure 9. HR-SEM images of (a) mesoporous Pt, (b) $Pt_{86}Ru_{14}$ alloy, and (c, d) $Pt_{62}Ru_{38}$ alloy fibers synthesized from the precursor solutions with metal compositions of (a) Pt_{100}, (b) $Pt_{80}-Ru_{20}$, and (c, d) $Pt_{20}-$-Ru_{80}. The dashed lines in (d) indicate a partial ordering of mesostuctures. The scale bar is 30 nm.

phenomena were observed when other processes (e.g., microwave-assisted polyol and hydrosilylation processes) were applied.[25] The EDS mapping of the $Pt_{86}Ru_{14}$ fibers (prepared from $Pt_{80}Ru_{20}$ precursor solution) is shown in Figure 8e. The dark-field (DF) STEM image completely corresponded to the images of the EDS mapping of Pt and Ru. No phase separations in a nanometer scale were observed. Consequently, we can conclude by combinational characterizations that the Pt−Ru fibers were in the intermetallic alloy state.

Ru fibers from Ru-based LLCs have mesoporous structures that are quite different from those of other mesoporous Pt and Pt−Ru fibers. The TEM and HR-SEM images show that the uniform-size mesopores are randomly packed to make a 3-dimensional (3D) mesoporous structure, though the LLCs had a 2D-hexagonal structure (Figure 10). The mesopore size is around 3 nm, in good agreement with the size of the self-assemblies consisting of $C_{16}EO_8$ surfactants.[7a,7f] Such a 3D mesoporous structure is thought to be deposited from either micellar cubic (I_1) or bicontinuous cubic (V_1) as a template, based on the $C_{16}EO_{10}$-type LLC phase diagram.[19] At present, the transition of the LLCs is conceivable. It was reported that, as the concentration of metal ions dissolved in LLCs was gradually decreased, the transition from the micellar cubic (I_1) phase to the 2D-hexagonal (H_I), bicontinuous cubic (V_1), and lamellar (Lα) phases occurred.[19] Therefore, as the Ru deposition in LLCs proceeded, the Ru ion concentration decreased, which induced the transition from the 2D-hexagonal (H_I) to the bicontinuous cubic (V_1) phase. Although the phase boundaries were changed by surfactants and dissolved metal ions, in the case of the Ru-based LLCs, the transition might have occurred at a very early stage of deposition. Therefore, no mesostructures derived from a 2D hexagonal LLC phase were observable in most fibers.

The nanoparticle size in the framework was less than 1.5 nm, smaller than that of other mesoporous Pt and Pt−Ru alloy fibers (Figure 9). In addition, the ED showed weak ring-like patterns assignable to the Ru hcp structure (Figure 10b). No intense spots were confirmed, indicating that the domain sizes of Ru crystals were dramatically decreased. In fact, the lattice fringes were randomly oriented (Figure 10c). In general, Ru has an hcp structure at room temperature. As reported previously, when the same synthetic conditions were applied, Ru nanoparticles were smaller than Pt nanoparticles.[26] A similar situation was found in the current study. The XPS study described above (Figure 6d) indicated that the 25 at % Ru atoms in the fibers were oxidized. A large number of Ru atoms exposed on the surface of the fibers were likely oxidized because Ru atoms are easily oxidized under atmospheric conditions. The size reduction of the nanoparticles assembled in the frameworks likely accelerated the oxidation of the surface. Although direct templation from the original 2D hexagonal LLCs failed, this is the first report of mesoporous Ru/Ru oxides from lyotropic liquid crystals. By further optimization of LLC compositions, successful direct templation from original LLC structures without an LLC phase transition will become possible.

The electrochemical oxidation of the adsorbed CO on the mesoporous fibers in 0.5 M H_2SO_4 is shown in Figure 11. The peak potentials for oxidation of the CO monolayer for mesoporous Pt, $Pt_{96}Ru_4$ (prepared from $Pt_{90}Ru_{10}$ LLCs), $Pt_{86}Ru_{14}$ (prepared from $Pt_{80}Ru_{20}$ LLCs), and Ru fibers were about 0.74, 0.65, 0.62, and 0.60 V, respectively. With an increase in the Ru content, the threshold and peak potentials were shifted to lower electrode potentials. This phenomenon supports the incorporation of the Ru content into the fibers.[26] Using the probe value of 420 μC cm^{-2} for the stripping of a CO monolayer, the electrochemically active surface areas measured from the CO stripping charge were 16, 20, 23, and 62 m^2 g^{-1} (Table 1). The value of mesoporous Pt fiber was close to those reported for 2D-hexagonally ordered mesoporous Pt films and particles from LLC phases with the same surfactants ($C_{16}EO_8$), ranging from 17 to 23 m^2 g^{-1}.[7a,7b] The gradual increase of the surface areas

(26) (a) Takasu, Y.; Fujiwara, T.; Murakami, Y.; Sasaki, K.; Oguri, M.; Asaki, T.; Sugimoto, W. *J. Electrochem. Soc.* **2000**, *147*, 4421–4427. (b) Takasu, Y.; Sugimoto, W.; Murakami, Y. *Catal. Surv. Asia* **2003**, *7*, 21–29.

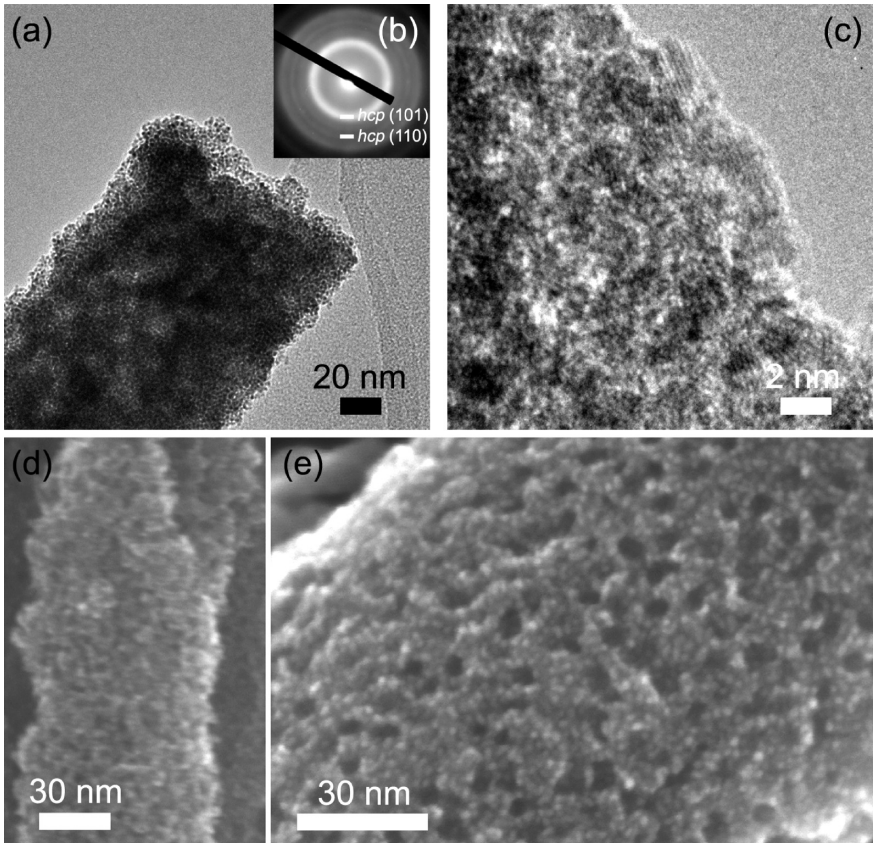

Figure 10. TEM and HR-SEM images of mesoporous Ru fibers. (a) Low-magnified TEM image. (b) Selected-area ED patterns. (c) Highly magnified TEM image. (d, e) HR-SEM images.

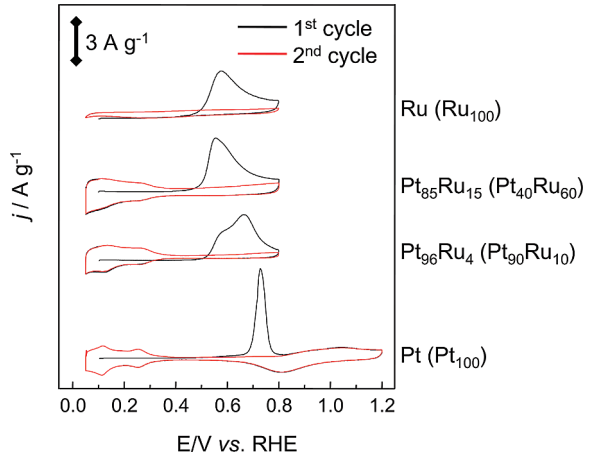

Figure 11. Cyclic voltammograms of the electro-oxidation of preadsorbed CO on mesoporous fibers. The product compositions are noted. The compositions shown in parentheses indicate the LLC compositions.

was attributed to the increase in the lighter-element Ru in the fibers and the reduction of the nanoparticle size in the framework.

The performance of fuel cells such as DMFCs is strongly dependent on the electrocatalysts used. Accordingly, for the best DMFC performance, it is highly desirable and perhaps technologically necessary to develop good electrocatalysts to explore the performance of methanol electro-oxidation. The electrocatalytic properties of the mesoporous fibers with various Ru contents toward the methanol electro-oxidation reaction were

Table 1. Electrochemical Analysis Data

composition of products (LLC composition)	electrochemically active surface areas ($m^2\ g^{-1}$)	mass-normalized catalytic activity (A (g of metal)$^{-1}$)
Pt (Pt_{100})	16	1.6
$Pt_{96}Ru_4$ ($Pt_{90}Ru_{10}$)	20	2.5
$Pt_{85}Ru_{15}$ ($Pt_{40}Ru_{60}$)	23	12
Ru (Ru_{100})	62	0.0

evaluated from the quasi-steady-state current density at 0.50 V in 0.5 M H_2SO_4 solution containing 1 M methanol at 60 °C. The catalytic activity increased with an increase in the Ru content, but mesoporous Ru had no catalytic activity (Table 1). The $Pt_{85}Ru_{15}$ fibers (prepared from $Pt_{40}Ru_{60}$ LLCs) exhibited the highest mass specific current density of 12 A (g of metal)$^{-1}$. The high mass-specific activity of mesoporous Pt−Ru alloy fibers was attributed to the high surface area (i.e., high number of active surface metal sites). The alloying with Ru further enhanced the electrochemical activity. The electrochemical properties of 30 mass% $Pt_{50}Ru_{50}$ supported on Vulcan Carbon ($Pt_{50}Ru_{50}$/C) were characterized for comparison. The electrochemically active surface area of $Pt_{50}Ru_{50}$/C was 65 m^2g^{-1} and its mass activity was 52 A (g of metal)$^{-1}$, which are a few times larger compared to those of $Pt_{85}Ru_{15}$ fibers (prepared from $Pt_{40}Ru_{60}$ LLCs) in this study. The difference in the electrochemical characteristics of the present mesoporous PtRu fibers is reasonable if considering the nonsupported nature. Naturally,

supported materials afford higher surface areas and activities compared to nonsupported bulk catalysts.

4. Conclusion

We successfully synthesized mesoporous Pt−Ru fibers via the EDIT method using diluted precursor solutions, including the Pt and Ru species. Tunable controls of Pt and Ru ratios were realized by changing the composition of Pt and Ru in precursor solutions. The Pt and Ru were uniformly dispersed in the fibers and were rarely oxidized. By detailed characterizations using HR-SEM and TEM observations, EDS mapping, and XPS analysis, it was proved that the Pt and Ru in the fibers were in the intermetallic alloy state. In addition, the obtained mesoporous fibers had unique stacked donut-like mesochannels due to the confined effect of the PAAM channels. Because macrospaces were created among the fibers, macro-meso-type hierarchical structures were formed, providing more efficient diffusions of the guest species and electrolytes. Furthermore, the mesopore walls consisted of connected nanoparticles in crystalline alloy states. Consequently, multiple controls on the macroscopic (morphologies), mesoscopic (mesochannel orientations), and atomic levels were achieved simultaneously through our dual-templating method using both LLCs and PAAMs. We strongly believe that our method can provide an important platform for the fabrication of next-generation high-performance electrodes, electrocatalysts, and biosensing materials.

Acknowledgment. The authors acknowledge Mr. M. Fuziwara (Waseda University) and Dr. Y. Nemoto (NIMS) for TEM observation and Mr. Y. Kanno (Waseda University) for 2D-XRD measurement. The present study was supported by the Global COE Program "Practical Chemical Wisdom" from the Japanese Ministry of Education, Culture, Sports, Science, and Technology (MEXT). This work was also supported by the A3 Foresight Program "Synthesis and Structural Resolution of Novel Mesoporous Materials" from the Japan Society for the Promotion of Science and by a Grant-in-Aid for Scientific Research (19850031) from JSPS. A.T. is grateful for financial support provided through a Grant-in-Aid for JSPS Fellows from MEXT.